The effect of microstructure on the temperature dependence of the interlayer coupling in Co/Cu multilayers

C. Christides[a)]
Department of Engineering Sciences, School of Engineering, University of Patras, 26 110 Patras, Greece

(Received 29 March 2000; accepted for publication 22 June 2000)

Three classes of giant magnetoresistance Co(1 nm)/Cu(2.1 nm) multilayers were sputter grown with different microstructures in respect to grain size and interface roughness, depending on deposition conditions. Magnetization and current in-plane giant-magnetoresistance (GMR) isothermal loops reveal an unusually high increase of coercivity from 280 down to 5 K. In addition, a systematic variation was observed in the temperature dependence of the indirect exchange coupling as the Co–Cu layering is modified in the three classes of Co/Cu multilayers. Specifically, the temperature dependence of the saturation (switching) field in the GMR-loops, and the indirect coupling strength, vary as $(T/T_0)/\sinh(T/T_0)$ whereas the spin-blocking temperature T_0 is found equal to 84(4), 96(11), and 105(10) K for class *A*, *B*, and *C* multilayers, respectively. These results indicate that the desirable low hysteresis appears in the GMR loops at room temperature because the spin structure becomes unstable above the obtained T_0 due to domain wall fluctuations. Such magnetic fluctuations define a short–range order state above T_0 that depends on Co–Cu intermixing and geometric factors of the grains. © *2000 American Institute of Physics.* [S0021-8979(00)03619-7]

I. INTRODUCTION

Since the first reports[1] for enhanced giant-magnetoresistance (GMR) amplitudes in Co/Cu multilayers (MLs) the related research has been focused on the interlayer exchange coupling mechanism[2–6] and the possible applications of Co/Cu GMR devices. The maximum GMR amplitude ($\approx 60\%$) at ambient conditions was observed in sputtered (polycrystalline) Co/Cu MLs[1] with (111) texture whereas its GMR ratio and bilinear exchange coupling strength J_{osc} oscillate with decaying amplitude as the Cu layer thickness (t_{Cu}) varies, giving maxima that correspond to antiferromagnetic (AF) coupling between adjacent Co layers. Thus when these MLs are of such thickness as to be AF coupled then a reduction of the magnetoresistance occurs if they are subjected to a magnetic field parallel to the interfaces, whereas a minimum value is observed at a saturation (or switching) field H_s where the spins between adjacent magnetic layers come into alignment.

The large GMR ratios and the relatively large sensitivity to changes in magnetic fields, observed at the first two AF maxima with $t_{Cu} \approx 0.9$ and 2 nm, make these MLs potential candidates for use in sensor devices.[7,8] However, the undesirable hysteresis that appears in the GMR response function of the first and second AF maximum requires modification of the Co/Cu composition[9,10] and of the film morphology[11] in order to achieve negligibly small hysteresis while maintaining adequate sensitivity for sensors. The possible technological applications,[12] that can emerge from the large GMR ratios observed in polycrystalline MLs with (111) texture, attract a great deal of scientific interest to investigate the elusive mechanism between the microscopic origin of the GMR phenomenon and the film morphology.

For GMR sensor applications, besides the GMR ratio and the switching field range, equally important is the signal-to-noise ratio as well. The excessive flicker or $1/f$ noise has been found[13] to be of magnetic origin in GMR sensors. The source of this excess noise level with the applied dc-field H has been attributed[13] to thermal excitations of the magnetization direction. Therefore, the physical origin that creates low hysteresis in the GMR response function should also affect the $1/f$ contribution that depends on[13] the applied dc-magnetic field.

Earlier studies[9,10] in GMR Co/Cu MLs at the second AF maximum, that exhibit low-hysteresis at about 290 K, have shown a dramatic increase of hysteresis below 100 K. These results imply that, while the activation energy for magnetization reversal is reduced by a decrease of Co layer thickness[9] (t_{Co}) or by Co–Cu alloying,[10] it remains large relative to thermal energy at low temperatures. So far the properties of the micromagnetic state, that reduce hysteresis in the GMR loops at room temperature, are unknown.

The aim of the present study is to investigate the micromagnetic properties that result in low-field GMR by measuring the temperature dependence of isothermal magnetic and GMR loops in three classes of $[\mathrm{Co}(1\ \mathrm{nm})/\mathrm{Cu}(2.1\ \mathrm{nm})]_{30}$ MLs between 5 and 300 K. Such macroscopic measurements include combined magnetostructural information. However, micromagnetic parameters such as lateral magnetic correlation length and roughness vary with temperature and are totally different[14,15] from the corresponding microstructural parameters which remain unaltered in the examined temperature range. A previous study[11] has shown that these three classes exhibit different GMR ratios, hysteresis, and

a)Electronic mail: christides@ims.demokritos.gr

saturation fields at room temperature as the Co–Cu layering is modified by the deposition conditions. The t_{Cu} was selected at the second AF maximum in order to avoid such micromagnetic effects on hysteresis loops as those observed[16] at the first AF maximum, due to growth of pinhole defects and FM bridges in the multilayer structure. Since Co/Cu interface roughness affects primarily the interlayer exchange coupling whereas the grain size distribution and the density of grain boundaries alter the magnetostatic energy then the temperature dependence of GMR and magnetic hysteresis loops can separate the major contribution from each one of the two structural characteristics.

II. EXPERIMENTAL DETAILS

Three different microstructures of $[\mathrm{Co}(1\,\mathrm{nm})/\mathrm{Cu}(2.1\,\mathrm{nm})]_{30}/\mathrm{Co}(1\,\mathrm{nm})$ MLs were deposited by magnetron sputtering on Si(100) substrates, as described in Ref. 11. Their microstructure is different in respect to grain size and interface roughness, depending on the deposition conditions.[11] An outline of the specific differences in preparation is given here for a solid presentation of this work. Two parameters were varied to produce the three classes (named *A*, *B*, and *C*) of Co/Cu multilayers: (i) the surface roughness of the Si(100) substrate, affecting the mode of growth; (ii) the thermal contact of the substrate with the water cooled, supporting table that influence internal film stress. The base pressure (3×10^{-7} Torr), deposition rates, and the Ar-gas purity (99.999%) were the same. Thus, class *A* multilayers were grown on 100 nm SiO_2 buffer layer with less than 2 nm root-mean-square (rms) surface roughness and direct contact of the substrate with the supporting table. Class *B* has the difference that the substrate was thermally isolated from the water cooled supporting table (extra internal stress), whereas class *C* has in addition a rougher (rms more than 3 nm) surface of the substrate. Transmission electron microscopy (TEM) measurements[11] have revealed column-like structures with bimodal distribution of grain sizes. A 90% fraction of columnar grains with sizes more than 15 nm is observed in the sample called *A*, for sample *B* it is 70%, and in sample *C* is less than 50%. Thus a larger fraction of grains with sizes less than 10 nm appears progressively from sample *A* to *C*.

X-ray reflectivity (XRR) measurements were performed with a Rigakou diffractometer, using Cu $K\alpha_1$ radiation from a 30 kW rotating anode source and a RINT2000 wide angle goniometer. The XRR scans were collected at ambient conditions between 0.400° and 8.000° with a step angle of 0.008°, an 0.05 mm incident-beam divergence slit and a receiving slit of 5.0 mm. To obtain specular reflectivity conditions the film was aligned by tracking first the grazing incident beam on the sample and afterwards the reflected beam.[17] Magnetic hysteresis and GMR loops were measured with a Quantum Design MPMSR2 superconducting quantum interference device (SQUID) magnetometer between 5 and 300 K. The GMR measurements were performed with the four-point-probe method using a dc current of 10 mA. All measurements were performed by first applying the maximum positive field *H* parallel to current flow direction and then completing the loop.

III. EXPERIMENTAL RESULTS

A. Structural characterization

It is instructive to summarize the conclusions drawn from micro- or macrostructural techniques applied in previous studies of these multilayers. The x-ray diffraction patterns of class *A*, *B*, and *C* MLs exhibit an intense face-centered-cubic (fcc) (111) Co–Cu peak and a weak (200) fcc peak, indicating that the MLs have (111) texture. Selected-area electron diffraction (SAED) planar TEM patterns have shown[11] that at right angles relative to Si surface there is not any preferred orientation of the (111) Co–Cu planes for all the examined MLs. However, for samples *A* and *B* the SAED cross-section patterns show[11] that there is some degree of preferred orientation in the (111) Co–Cu planes relative to the Si [200] direction only, whereas in class *C* MLs they are randomly arranged. Since bulk Co and Cu layers have similar densities ($\approx 8.9\ \mathrm{g/cm^3}$) the small x-ray contrast results in weak satellite intensities around the foundamental (111) Bragg peak which does not allow a superlattice refinement (SUPREX program) analysis as[18] in Co/Au MLs. It should be emphasized that in previous studies the microstructure of class *A*, *B*, and *C* MLs has been identified by TEM measurements[11] whereas class *B* MLs have been characterized with nondestructive methods such as[18] spin-echo ^{59}Co nuclear magnetic resonance (NMR) (microscopic technique)[18] and XRR measurements[19] (macroscopic technique) as well. To extract some conclusions about the quality of Co/Cu interface roughness high resolution XRR measurements on class *A* MLs are compared with XRR spectra taken in class *B* MLs.[19]

Figure 1 shows the specular XRR spectrum from class *A* MLs. An attempt to fit the experimental spectrum either with an optical or a kinematical model[19] gave poor fittings. This indicates that, due to incoherent absorption (anomalous dispersion effects) in the layer materials when Cu $K\alpha$ radiation is used, a sophisticated dynamical model[20] is required for a reliable fitting of the observed spectrum. However, the quality of the recorded spectrum allows a straightforward interpretation of the main structural features because there were not detectable geometrical aberration effects[17] introduced by the sample curvature. The first two ($m=1,2$) superlattice Bragg peaks appear very intense with small full width at half maximum, indicating sharp Co/Cu interfaces. In comparison, the XRR spectra observed[19] in class *B* MLs did not show superlattice Bragg peak intensities of the $m=2$ or higher order and the amplitude of the interference fringes was suppressed, indicating that interface Co–Cu roughness is larger. It is worth mentioning that the zero peak intensity of the third order ($m=3$) satellite in Fig. 1 shows unambiguously that both, the achieved t_{Cu} and the bilayer thickness Λ, correspond exactly at the position where the maximum GMR ratio is expected at the second antiferromagnetic maximum of Co/Cu MLs because

$$\Lambda = t_{Cu} + t_{Co} \quad \text{and} \quad t_{Cu} \approx 2t_{Co} \Rightarrow \Lambda \approx (3/2)t_{Cu} \tag{1}$$

and the angle-depependent structure factor $F(\theta_m)$ at the Bragg-angle θ_m becomes[21]

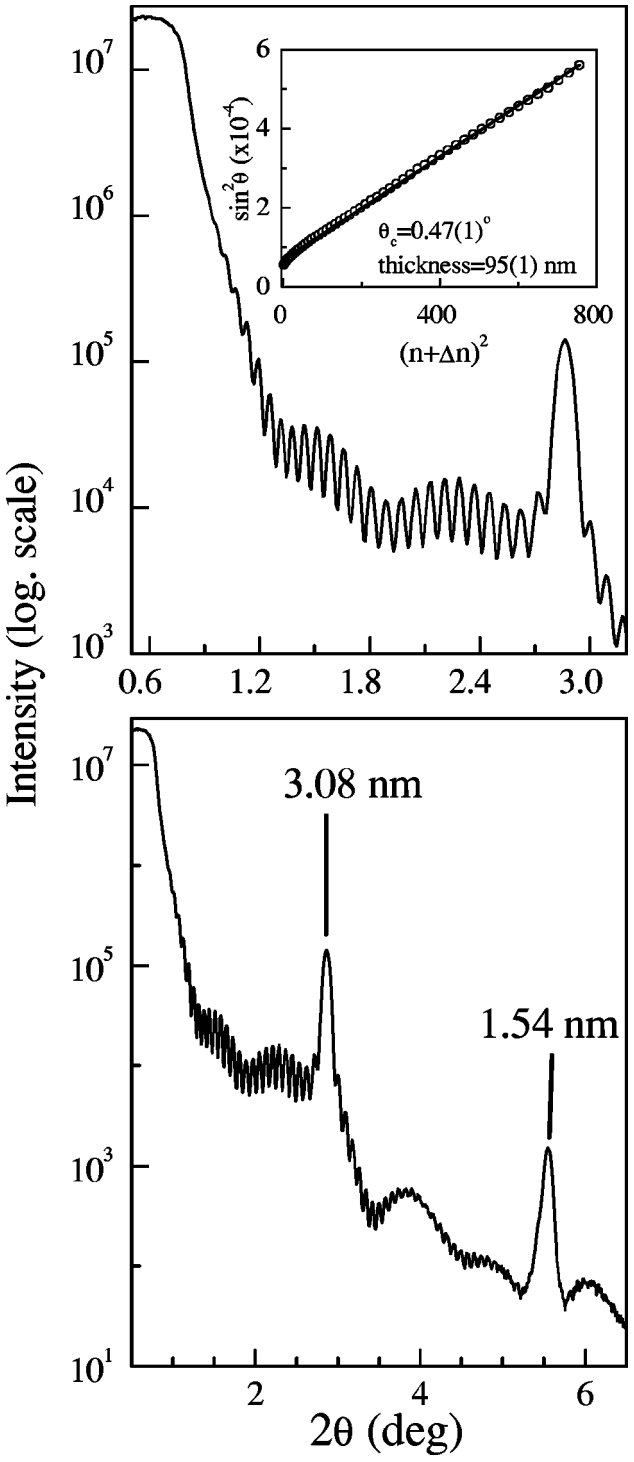

FIG. 1. The bottom plot shows the XRR spectrum from class *A* MLs whereas the plot on top shows an enlargement of the spectrum, with a clear view of the interference fringes used in the calculations. The inset shows the θ_i positions (circles) used in Eq. (3) and the best fit line.

$$F(\theta_m)=\frac{\Lambda}{\pi m}\sin\left\{\frac{m\pi t_{\mathrm{Cu}}}{\Lambda}\right\}(\phi_{\mathrm{Cu}}-\phi_{\mathrm{Co}})\overset{(1)}{\Rightarrow}F(\theta_m)$$

$$=\frac{3t_{\mathrm{Cu}}}{2\pi m}\sin\left\{\frac{2m\pi}{3}\right\}(\phi_{\mathrm{Cu}}-\phi_{\mathrm{Co}})=0 \quad \text{if} \quad m=3,6,..., \quad (2)$$

where ϕ_{Cu} and ϕ_{Co} are the scattering amplitude densities for x rays of a particular wavelength λ. The fact that t_{Cu} and Λ are exactly at the second GMR maximum position makes meaningful the analysis of the observed temperature dependence in the following sections.

Other important differences in film morphology can be traced from XRR spectra by measuring the critical reflection angle θ_c. Beyond the region for total reflection (plateau) the maxima and the minima of its interference fringes can be related to the total film thickness t_f by the modified Bragg equation[22]

$$\sin^2\theta_i=\theta_c^2+(n_i+\Delta n)^2\lambda^2/4t_f^2, \quad (3)$$

where θ_i is the position of the maximum or minimum intensity of the ith interference fringe, n_i is an integer, Δn is 1/2 and 0 for maximum and minimum, respectively. The insert in the upper part of Fig. 1 shows data for the refinement of forty minima and maxima of well defined interference fringes between 1.20° and 2.72° in θ. A $t_f=95(1)$ nm and a $\theta_c=0.47(1)°$, with numbers in parantheses being the standard deviations, are obtained by least-squares refinement (solid line) of the θ_i positions using Eq. (3). The difference between the nominal (=94 nm) and the estimated t_f is within the accuracy of the standard deviation limits ($\sim 1\%$) while the Bragg-peak positions (Fig. 1) give a $\Lambda=3.08$ nm. However, the estimated electron density $\rho_e=12.4$ g/cm^3 from the obtained $\theta_c(\sim\sqrt{\rho_e})$ is much larger than the bulk Cu or Co density of about 8.9 g/cm^3, which correspond to a $\theta_c \approx 0.4°$. Since the observed interference fringes indicate a small rms interface roughness, then the over-estimation of θ_c (ρ_e) by the modified Bragg equation may arise from the different reflectivities reported[23] between interfaces with small and large values of the lateral correlation length ξ. The difference between surfaces with small and large values of ξ can be a factor of two in specular reflectivity, whereas for $\xi>100$ nm an ill-defined θ_c region appears.[23] In accordance, atomic force microscopy measurements[11] on the substrate surface prior deposition and on the film surface revealed that class *A* MLs have atomically smooth substrate–film interfaces whereas both surfaces exhibit a long-range waviness with average periodicity of about 100 nm. Thus the over-estimated θ_c can be attributed to large ξ.

In contrast a detailed XRR study of class *B* MLs has shown[19] that both, Co/Cu interface and lateral correlation function $C(\xi)$ roughness are governing their layer morphology, while TEM measurements[11] show that class *C* MLs exhibit a large geometrical and chemical (Co–Cu mixing) roughness. Thus, increase of film roughness from class *A* to *C* MLs is an unavoidable result of the larger fraction of small grain sizes that changes the overall film morphology. However, increase of Co/Cu interface rougnhess weakens the magnitude of interlayer exchange coupling within each columnar structure whereas a larger fraction of small grains makes the magnetostatic contribution an important dipolar energy term in the total magnetic free energy that determines the micromagnetic state of the film. In the following sections it will be shown that the two different magnetic contributions in the GMR and magnetization hysteresis loops can distinguish the effect of interface roughness from grain size effects in the temperature dependence of the two data sets.

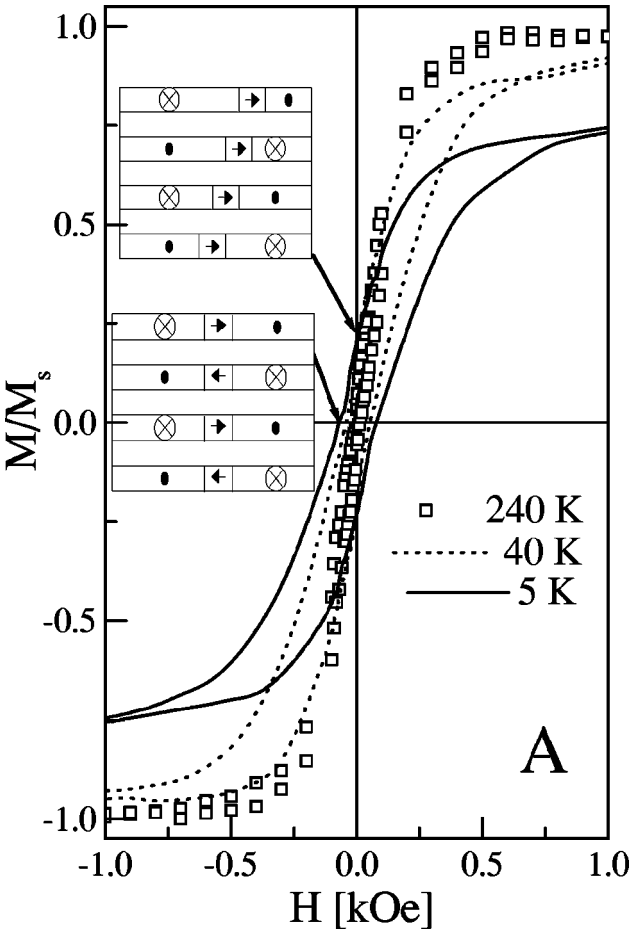

FIG. 2. The isothermal M/M_s-H loops of class *A* MLs are shown for clarity at three different temperatures only. Schematic views of the proposed domain structures are shown at the remnant (upper plot) and demagnetized (down plot) states.

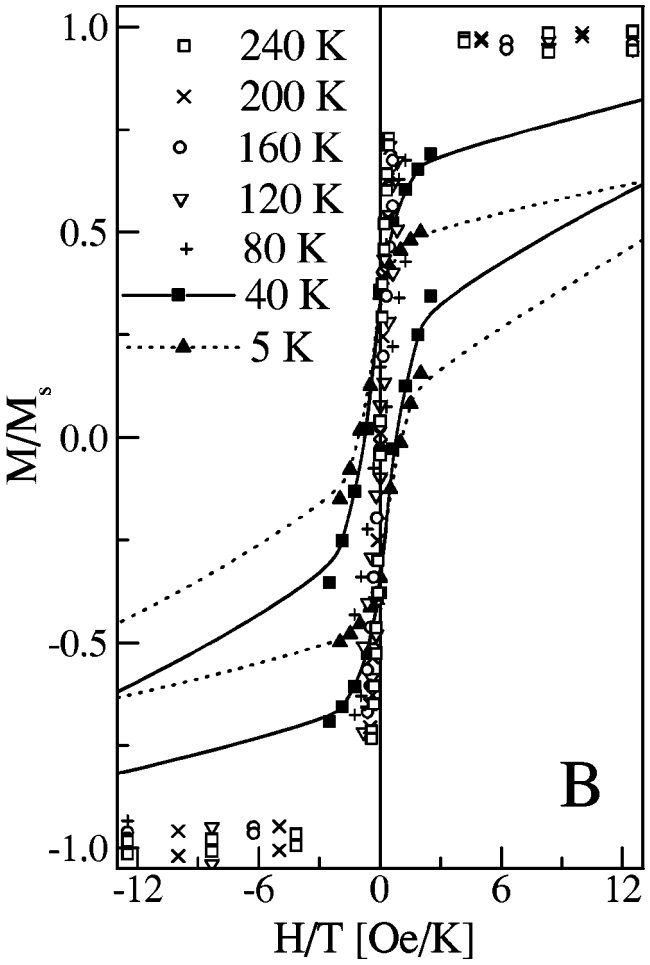

FIG. 3. The isothermal M/M_s-H loops of class *B* MLs are shown as a function of temperature. The lines are guides to the eye.

B. Magnetic measurements

Isothermal magnetization loops were measured between 5 and 280 K. Figure 2 shows normalized magnetization (M/M_s-H) loops, with M_s being the total saturation magnetization, of sample *A* at 240, 40, and 5 K. The temperature dependence of the M/M_s-H loops reveals a large increase of coercivity (H_c) and saturation (H_s) fields below 80 K. Above 200 K there is a negligibly small remanent magnetization (M_r) and the loop shapes indicate an antiparallel alignment of magnetic moments among adjacent Co layers at the demagnetized state ($M=0$). Since the temperature dependence of these loops is more prominent in class *B* and *C* MLs, the normalized magnetization curves were plotted (Figs. 3 and 4) as a function of the applied field over temperature ratio H/T. In nanostructured systems, that exhibit an increase of hysteresis by decreasing temperature while their intrinsic magnetic anisotropy is negligibly small, the M/M_s versus H/T plots reveal the thermal energy lacked from the magnetic configuration to complete equilibrium with the applied field during the measurement. A comparison of the observed loops in Figs. 2–4, reveal that

(i) Class *A* MLs (about 90% fraction[11] of AF-aligned layers) exhibit an $M_r<0.2\,M_s$ for all temperatures and the M_r increases at lower temperatures. This increase of M_r can be attributed either to creation of FM-coupled areas or to self-stabilization of magnetic domain walls in Co layers after the multidomain splitting from the saturated state.[24,25] In AF-coupled, sputter-grown, Co/Cu/Co sandwiches[25] a high domain density state is realized at remanence when coming from saturation. Also Co/Cu MLs grown by e-beam evaporation exhibit[26] minor GMR loops with higher GMR ratios than the major loops, indicating that domain wall effects are predominant around the remnant state. Thus a configuration with parallel Néel walls[27] (Fig. 2 inset) can account for the observed remanence in the case of the AF-coupled sample *A*. At the center of such Néel walls the average magnetic components point either parallel or antiparallel to each other between adjacent Co layers. Thus a larger fraction of Néel walls[27] with parallel moments can be stabilized in the remnant state of class *A* MLs with decreasing temperature. This effect is due to magnetization reversal by wall motion when a high field is applied and then removed.

(ii) In sample *C* the M_r values are lying in the range of $0.4\,M_s$ (280 K) $\leqslant M_r(T)\leqslant 0.8\,M_s$ (5 K) while for *B* are between $0.1\,M_s$ (280 K) $\leqslant M_r(T)\leqslant 0.4\,M_s$ (5 K). In these MLs the large M_r values cannot be explained by the magnetization reversal process that involves self- stabilization of Néel-type walls only. Since class *B* and *C* MLs contain different fractions[11] with small size columnar structures then

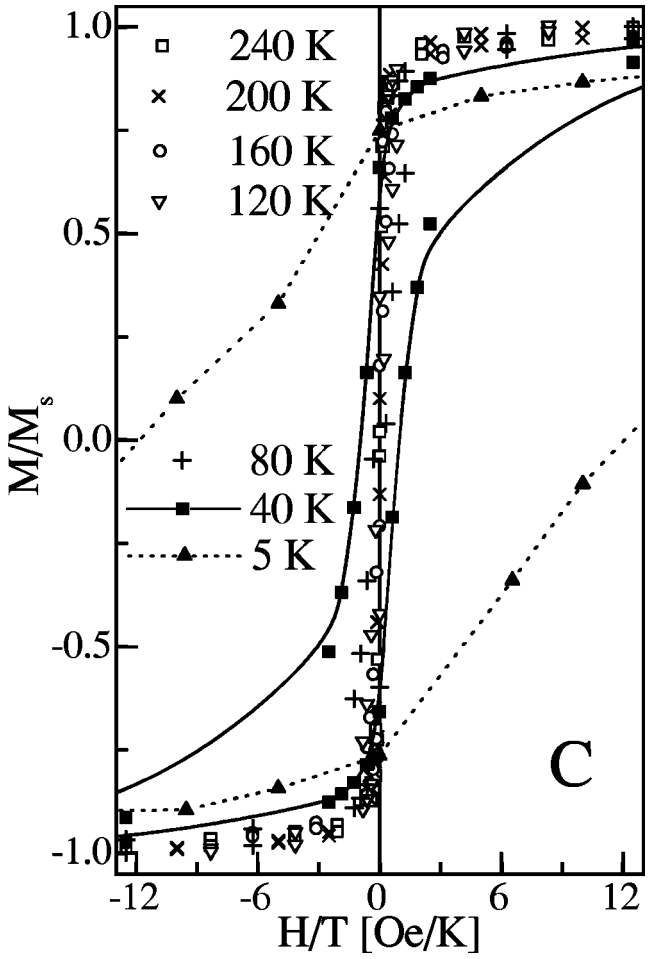

FIG. 4. The isothermal M/M_s-H loops of class C MLs are shown as a function of temperature. The lines are guides to the eye.

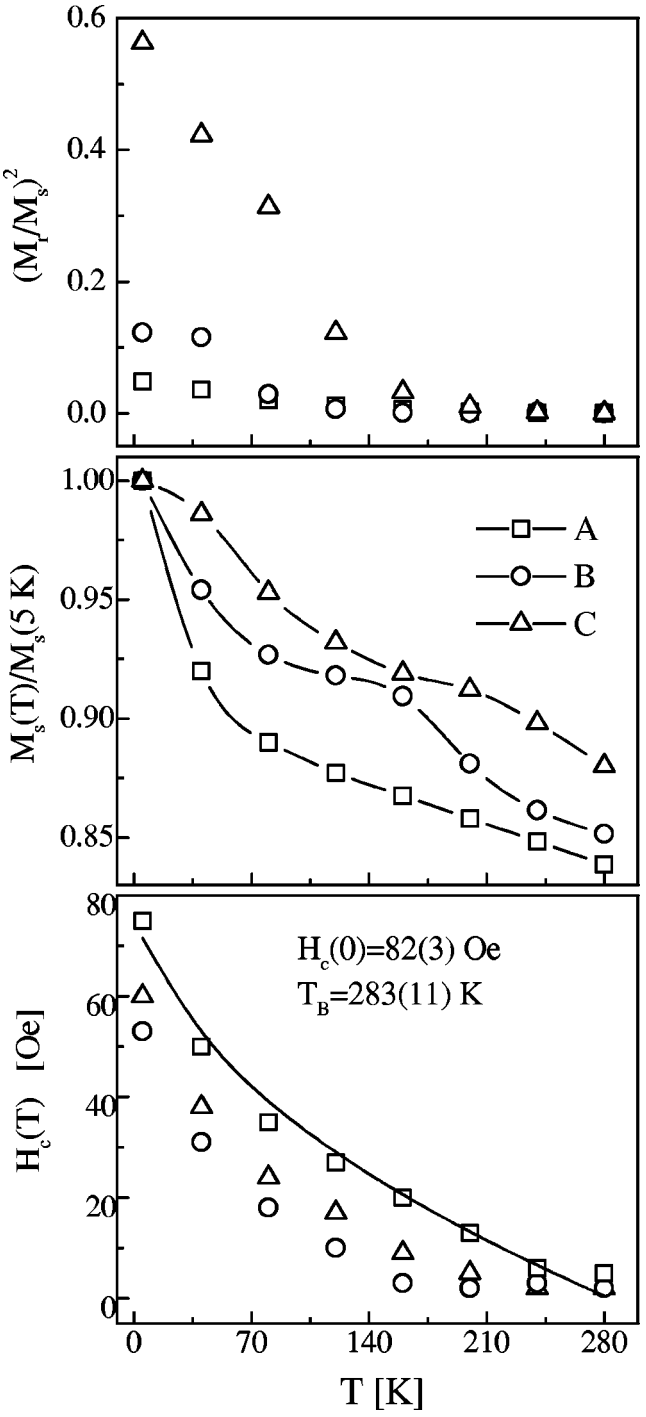

FIG. 5. The bottom plot shows the temperature dependence of the coercive H_c fields, obtained from isothermal M/M_s-H loops of classes A (□), B (○), and C (△) MLs. The solid line is the best fit using Eq. (4). The middle plot shows the temperature dependence of the normalized magnetization observed in class A, B, and C MLs. The lines are guides to the eye. The plot on top shows the temperature dependence of the square of the normalized residual magnetization M_r/M_s, observed in classes A, B, and C MLs.

minimization of the magnetostatic energy (long-range dipolar interactions) at grain boundaries results in FM-coupled areas nearby the small grains. Energy minimization of a Hamiltonian that involves short–range exchange and long–range dipolar interactions has produced[28] thermomagnetic curves for the uniform magnetization and the domain order parameter of ultrathin magnetic films that resemble those in Fig. 5 for certain grain sizes. Thus, it can be argued that a short–range-order state[28] appears at elevated temperatures, where the domain walls fluctuate infinitely. This can explain the observed decrease of M_r above 100 K in the three classes of MLs.

(iii) In sample C the number of required field-units per Kelvin (H/T) for the magnetization reversal process is much higher than that of sample B (Figs 3 and 4). This indicates that the larger fraction of small grains[11] in class C MLs is responsible for the magneting hardening at lower temperatures.

The normalized $M_s(T)/M_s$ (5 K), $[M_r(T)/M_s]^2$ and H_c values are plotted in Fig. 5 as a function of temperature for the three classes of MLs. Remarkably, the H_c is highest for the AF loop of sample A whereas the FM-like loops of sample C exhibit higher H_c values than sample B. Such effects can be explained by trapping of magnetic moments in local energy minima of individual grains that form an assembly with random orientations of magnetic easy axes.[29] Since the observed[11] variation in the bimodal distribution of grain sizes affects the short–range exchange, the long–range dipolar interactions and the anisotropy energy as we move from class A to C MLs, it may account for the different increase of H_c and M_r at lower temperatures as well. The most interesting result is revealed in the temperature dependence of mag-

netization which for the three classes of MLs does not follow the linear T, or $T^{3/2}$, or T^2 power laws. These laws were derived[5] for the cases of noncoupling, of FM and AF interlayer coupling, respectively, and observed[30,31] in fcc Co/Cu MLs at the first AF maximum, where the interlayer coupling term is dominant. The observed disagreement with these power laws in Fig. 5 is caused by the significant increase of M_s below 120 K. An enhancement of M_s induce a significant increase of the magnetostatic contributions in the long–range dipolar energy term which has not been taken into account in the minimization of the intrinsic magnetic free energy that leads to the specific power laws. Therefore, the intrinsic enhancement of M_s by decreasing temperature creates an extrinsic increase of magnetostatic dipolar interactions due to geometrical grain factors introduced by the specific microstructure. This extrinsic magnetostatic energy gives rise to a blocking temperature accompanied by significant increase of hysteresis below 120 K.

C. GMR results

Figures 6–8 show the temperature dependence of the GMR loops in the $H\|I$ configuration for class *A*, *B*, and *C* MLs, respectively. The large reduction of GMR effect—observed among class *A*, *B*, and *C* MLs—indicates that modification of the magnetic disorder at the Co–Cu interfaces, due to changes of roughness, alters the amount of spin-dependent scattering events. Usually, such effects result[32] in strong temperature dependence of the interlayer exchange coupling strength and the corresponding H_s in the GMR loops.

Accordingly, Fig. 9 shows that the GMR ratios $\Delta R/R_s = (R_{\max} - R_s)/R_s$, with $R_{\max}$ the maximum and R_s the minimum resistance at H_{peak} and H_s magnetic fields, respectively, follow a quasilinear decrease with increasing temperature for the three classes of MLs. Also Fig. 9 shows that the H_s exhibits a drop of more than 50% between 5 and 280 K, that evidences the strong sensitivity of the indirect coupling strength to temperature. These H_s values were estimated from the first derivative of the GMR curves, choosing the highest absolute values of field where the derivative line becomes horizontal. However, the most dramatic change occurs in H_{peak} values, where the three classes of MLs exhibit a steep increase below 100 K. This effect is similar to that observed in low-hysteresis GMR MLs with compositions:[9,10] $[\text{Co}(0.25\,\text{nm})/\text{Cu}(2\,\text{nm})]_{20}$ and $[\text{Co}_{0.5}\text{Cu}_{0.5}(1.1\,\text{nm})/\text{Cu}(2\,\text{nm})]_{20}$.

IV. ANALYSIS OF THE RESULTS

In AF-coupled Co/Cu MLs the demagnetized state at H_c can be achieved by domain-phase transformations during the application of a reverse field, that make more and more domains and domain walls to vanish.[25] Since the strength of H_c is associated with an intrinsic energy barrier that resists to magnetization reversal during demagnetization, it is more feasible to formulate its temperature dependence instead of calculating the normalized loops. The size of the columnar grains[11] indicates that parallel Néel walls can be stabilized near planar defects, such as columnar-grain boundaries,

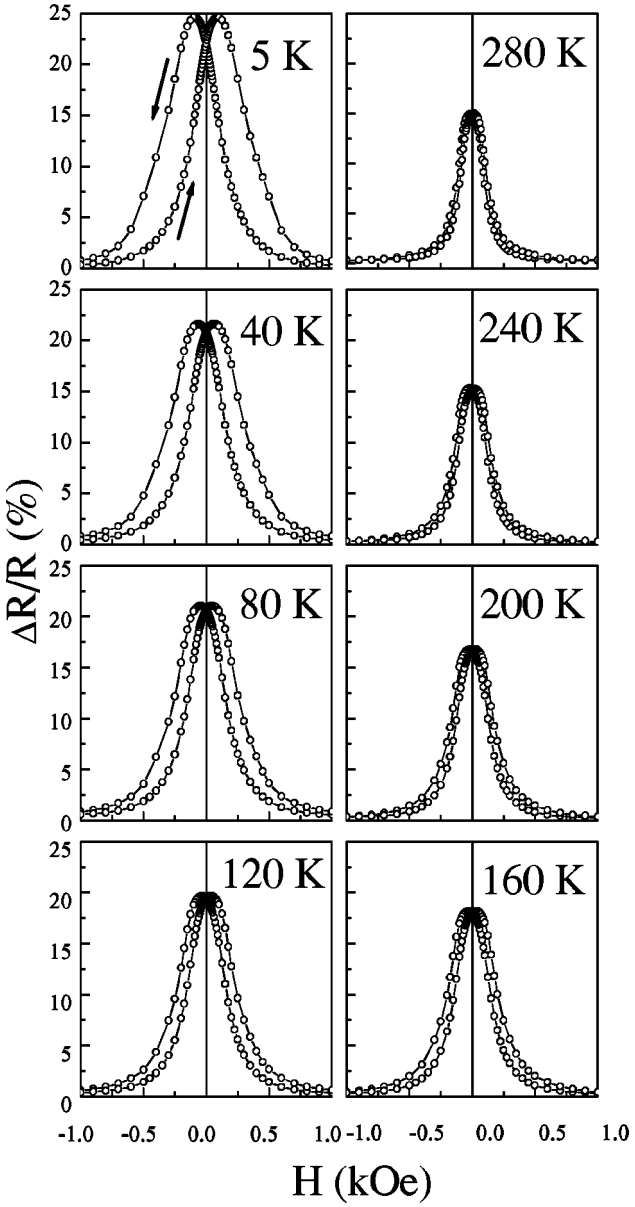

FIG. 6. The temperature dependence of the isothermal GMR loops is shown for class *A* MLs.

forming an assembly of noninteracting domains at the remnant state. Application of the same model as for magnetic nanoparticles can approximate[33] the temperature dependence of $H_c(T)$ by

$$H_c(T) = H_c(0)[1 - (T/T_B)^{1/2}], \tag{4}$$

where T_B defines a blocking temperature above which domain walls cannot be stabilized within the Co layers and the $H_c(T \geqslant T_B) = 0$. Since the involved phenomena concern the stability of micromagnetic states in polycrystalline MLs then, in principle, the magnetic ripple blocking or locking[34] mechanisms might be related to the physical origin of magnetization dispersion and the concept of T_B in Eq. (4). Equation (4) is used to fit the observed $H_c(T)$ values of sample *A* and the solid line in Fig. 5 (bottom plot) gives an $H_c(0) = 82(3)$ Oe and a $T_B = 283(11)$ K. As expected, Eq. (4) cannot fit the observed $H_c(T)$ values in class *B* and *C* MLs

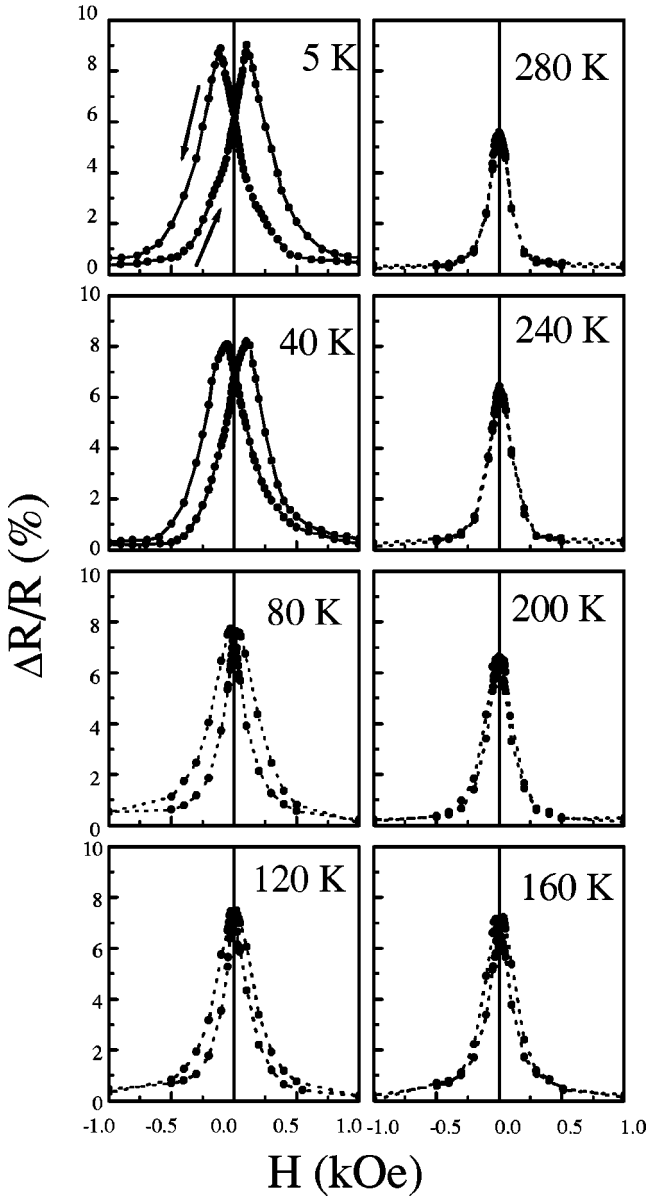

FIG. 7. The temperature dependence of the isothermal GMR loops is shown for class *B* MLs.

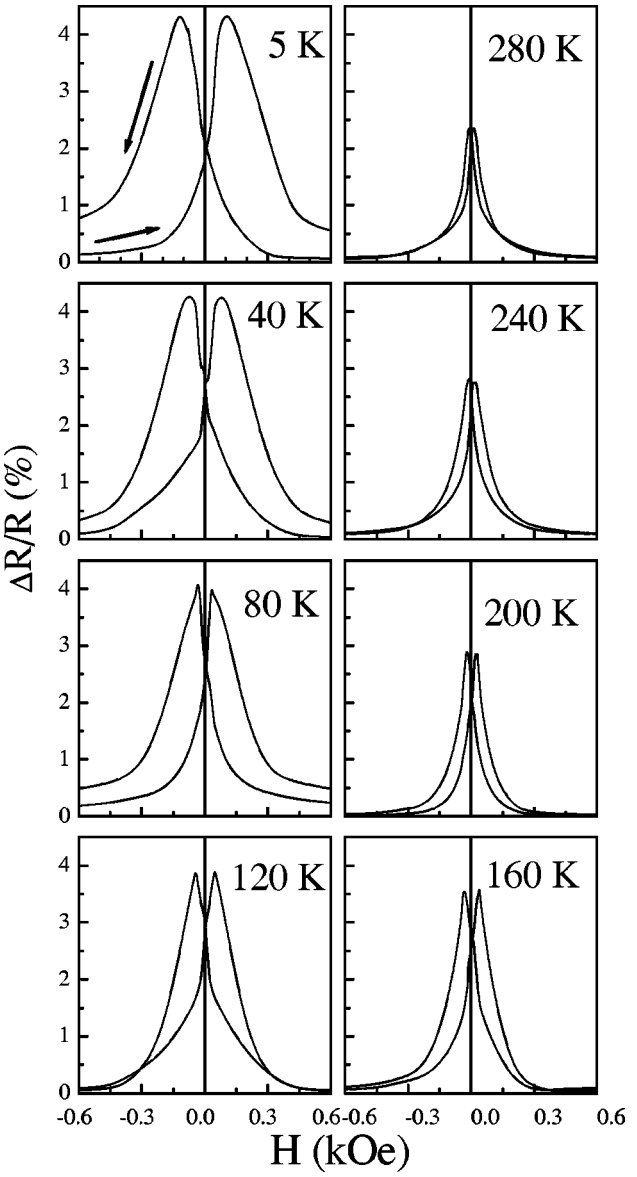

FIG. 8. The temperature dependence of the isothermal GMR loops is shown for class *C* MLs.

because a fraction of relatively small, FM-coupled, Co/Cu grains (not domain walls) coexists[11] with the larger, AF-coupled, columnar structures and the above approximations are not longer valid.

The observed variation of H_s and H_{peak} in Fig. 9 is comparable with the strong temperature dependence observed on a scale of about 100 K in[6] Co/Ru and[32] Co(hcp)/Cu MLs. Since the H_{peak} values (Fig. 9) depend primarily on the magnetization reversal process then they may follow the observed temperature variation of H_c (Fig. 5), that is derived from the isothermal M–H loops. Thus Eq. (4) was used to fit the H_{peak} values observed in class *A* MLs. The solid line in Fig. 9 is the best fit to square symbols, showing that Eq. (4) is a good approximation to H_{peak} variation as well. It is worth noting that an exponential function does not fit the observed temperature variation. The 20% difference of T_B values, obtained between the H_{peak} (Fig. 9) and H_c (Fig. 5) fits, indicate that a different thermal coefficient is involved in the second term of Eq. (4).

The most important result is related to the temperature dependence of H_s (Fig. 9) as the Co–Cu layering is modified in the three classes of Co/Cu MLs. So far, two different approximations were used to describe successfully the temperature dependence of H_s in AF-coupled MLs. The first assumes[4] that the temperature dependence originates from fluctuations in the spin angular momentum of the FM layers rather than from electronic effects in the spacer layers, resulting in an analytical expression for the fractional decrease of $H_s \sim T \ln T$, within the limits of spin-wave theory. The second approach assumes that the velocity of electrons v_F at the extremal points of the spacer Fermi surface (k_s) governs the temperature dependence of J_{osc} and the one-electron model[2] predicts for the fractional decrease of H_s that

$$[H_s(0)-H_s(T)]/H_s(0) \sim 1-[(T/T_0)/\sinh(T/T_0)], \quad (5)$$

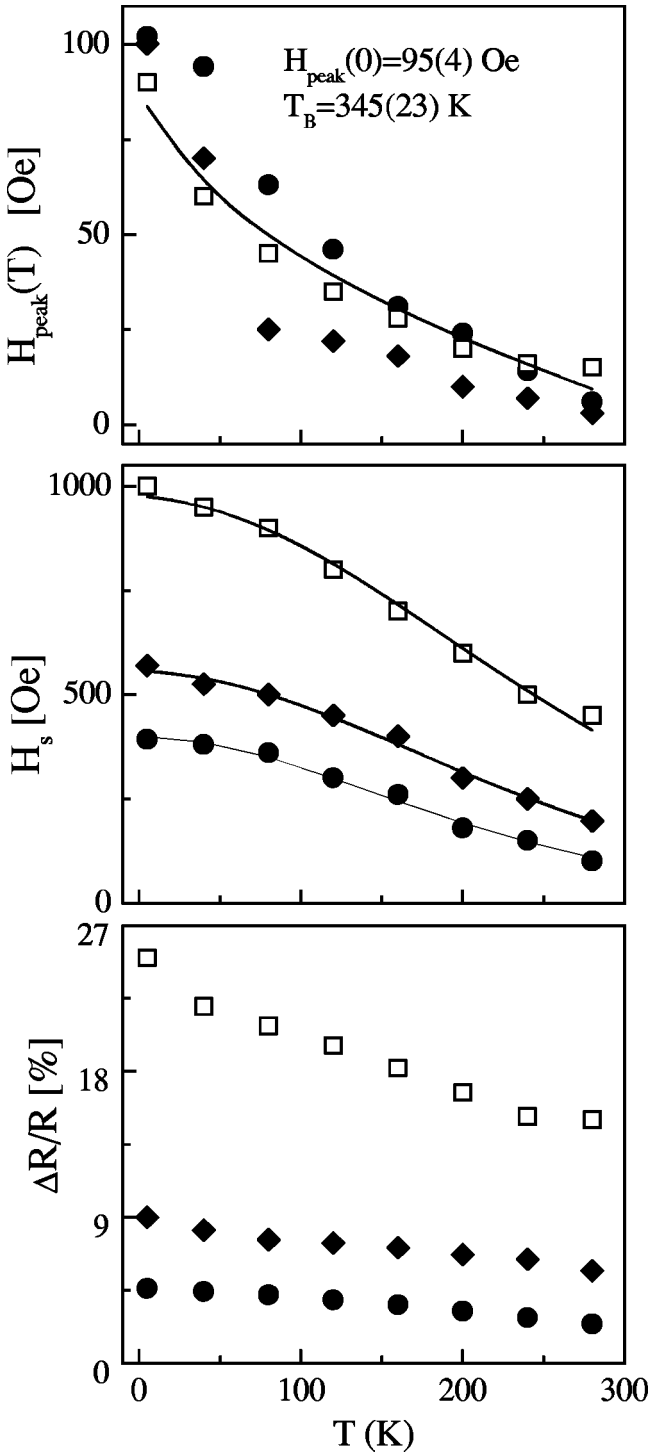

FIG. 9. The temperature dependence of H_{peak} (top), H_s (middle), and the GMR ratios (bottom)—obtained from the isothermal GMR loops of classes *A* (squares), *B* (diamond symbols), and *C* (solid circles) MLs—are shown. The solid line is the best fit of H_{peak} for class *A* MLs, using Eq. (4).

where the characteristic temperature T_0 is given by

$$T_0 = (\hbar v_F)/(2\pi k_s t_{Cu}). \quad (6)$$

Figure 10 shows that Eq. (5) fits the fractional decrease of H_s better than the $T \ln T$ function. This shows clearly that the Co/Cu interface roughness governs the temperature dependence of interlayer exchange coupling in the three classes of Co/Cu MLs. Earlier studies[2,6,32] indicate that T_0 is of the order of 100 K. In agreement, Fig. 10 shows that Eq. (5) fits the fractional decrease of H_s for classes *A* (crosses), *B* (triangles), and *C* (solid circles) MLs, using a T_0 of 84(4), 96(11), and 105(10) K, respectively.

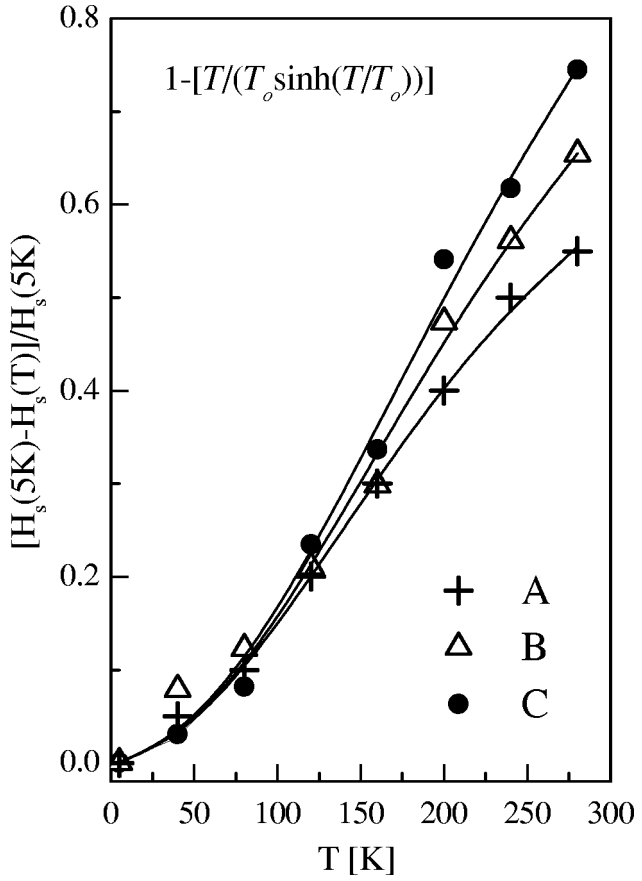

FIG. 10. The temperature dependence of the reduced saturation fields H_s, that were obtained from the isothermal GMR loops, are shown for classes *A* (crosses), *B* (triangles), and *C* (solid circles) MLs. The solid lines are the best fits using Eq. (5).

According to Eq. (6) the ratio v_F/k_s should increase as the T_0 values vary from 84 to 105 K and the Co/Cu interfaces become more disordered in class *B* and *C* MLs. However, it was observed[32] that the use of v_F of Cu in Eq. (6) gives theoretical T_0 values which are an order of magnitude larger than the experimentally observed. In Co[hexagonal-close-packed (hcp)]/Cu MLs the existence of either magnetically dead interfacial Co regions, that could modify the thermal evolution of the potential barrier, or fully confined magnetic carries in the spacer potential-well were proposed[32] as possible explanations for the strong temperature dependence of exchange coupling. It has been argued that[32] chemical roughness changes the spin-dependent potential barrier at the interfaces and alters the character of the electronic states near the Fermi surface. In agreement, the obtained variation of T_0 can be associated with a larger Co–Cu intermixing (chemical roughness) at the interfaces as we move from class *A* to *C* MLs.

V. CONCLUSIONS

The present study shows that the obtained differences among classes *A*, *B*, and *C* MLs are due to different degrees

of Co–Cu intermixing at the interfaces and to different geometric factors of the grains. Both are crucial for the obtained $(T/T_0)/\sinh(T/T_0)$ dependence of interlayer coupling because an increase of the fraction of small grain sizes increases the film roughness. However, the obtained increase of T_0 as we move from class *A* to *C* MLs can be understood only if we consider it as a thermal blocking or spin-freezing energy that depends on the concentration of Co loose spins near the interfaces, rather than as velocity of the carriers[2] at the stationery points of the spacer Fermi surface [Eq. (6)]. Thus, it is the thermal activation energy, which decouples magnetically the residual Co spins at the interfaces due to Co–Cu intermixing, that causes the desired lowering of H_s at room temperature.

On the other hand, it is the decrease of M_s from the magnetic decoupling of interfacial Co spins, which lowers the magnetostatic energy at grain boundaries above the T_B [Eq. (4)], that causes the desired softening of H_c and H_{peak} values observed in Figs. 5 and 9, respectively. Thus, the degree of H_c and H_{peak} softening scales with the density of grain boundaries (or the fraction of smaller grain sizes) present in the developed microstructure. The experimental results indicate that the spin structure of the examined Co/Cu MLs is not stable above the obtained T_0 or T_B values because the lowering of dipolar (magnetostatic) interactions[28,35] at grain boundaries can create a secondary short–range order state where domain walls fluctuate infinitely.

[1] S. S. P. Parkin, R. Bhadra, and K. P. Roche, Phys. Rev. Lett. **66**, 2152 (1991); S. S. P. Parkin, Z. G. Li, and D. J. Smith, Appl. Phys. Lett. **58**, 2710 (1991).
[2] D. M. Edwards, J. Mathon, R. B. Muniz, and M. S. Phan, Phys. Rev. Lett. **67**, 493 (1991).
[3] P. Bruno and C. Chappert, Phys. Rev. Lett. **67**, 1602 (1991); **67**, 2592 (1991); Phys. Rev. B **46**, 261 (1992).
[4] J. R. Cullen and K. B. Hathaway, Phys. Rev. B **47**, 14998 (1993).
[5] Z. Q. Qiu, J. E. Mattson, C. H. Sowers, U. Welp, S. D. Bader, H. Tang, and J. C. Walker, Phys. Rev. B **45**, 2252 (1994).
[6] Z. Zhang, L. Zhou, P. E. Wigen, and K. Quanadjela, Phys. Rev. B **50**, 6094 (1994).
[7] J. N. Chapman, J. Rose, P. A. Aitchison, H. Holloway, and D. J. Kubinski, J. Appl. Phys. **86**, 1611 (1999).
[8] C. Christides, S. Stavroyiannis, G. Kallias, A. G. Nassiopoulou, and D. Niarchos, Sensors Actuators **76**, 167 (1999).
[9] D. J. Kubinski and H. Holloway, J. Appl. Phys. **79**, 1661 (1996).
[10] D. J. Kubinski and H. Holloway, J. Appl. Phys. **82**, 322 (1997).
[11] C. Christides, S. Stavroyiannis, N. Boukos, A. Travlos, and D. Niarchos, J. Appl. Phys. **83**, 3724 (1998).
[12] M. Johnson, IEEE Spectr. **37**, 33 (2000).
[13] R. J. M. van de Veerdonk, P. J. L. Belien, K. M. Schep, J. C. S. Kools, M. C. de Nooijer, M. A. M. Gijs, R. Coehoorn, and W. J. M. de Jonge, J. Appl. Phys. **82**, 6152 (1997).
[14] J. F. MacKay, C. Teichert, D. E. Savage, and M. G. Lagally, Phys. Rev. Lett. **67**, 3925 (1996).
[15] J. W. Freeland, K. Bussmann, Y. U. Idzerba, and C.-C. Kao, Phys. Rev. B **60**, 9923 (1999).
[16] J. F. Bobo, H. Kikuchi, O. Redond, E. Snoeck, M. Piecuch, and R. L. White, Phys. Rev. B **60**, 4131 (1999).
[17] F. Bridou, J. Phys. III France **4**, 1513 (1994).
[18] C. Christides, S. Stavroyiannis, D. Niarchos, M. Wojcik, S. Nadolski, and E. Jedryka, Phys. Rev. B **59**, 8812 (1999).
[19] C. Christides, S. Logothetidis, M. Gioti, S. Stergioudis, S. Stavroyiannis, and D. Niarchos, J. Appl. Phys. **83**, 7757 (1998).
[20] T. Gu, A. I. Goldman, and M. Mao, Phys. Rev. B **56**, 6474 (1997); A. de Bernabé, M. J. Capitán, H. E. Fischer, and C. Prieto, J. Appl. Phys. **84**, 1881 (1998); Y.-P. Zhao, G.-C. Wang, and T.-M. Lu, Phys. Rev. B **55**, 13938 (1997).
[21] J. H. Underwood and T. W. Barbee Jr., Appl. Opt. **20**, 3027 (1981).
[22] T. C. Huang, R. Gilles, and G. Will, *Advances in X-Ray Analysis*, edited by J. V. Gilfrich *et al.* (Plenum, New York, 1994), Vol. 37, p. 183.
[23] D. K. G. de Boer, A. J. G. Leenaers, and W. N. van de Hoogenhof, J. Phys. III France **4**, 1559 (1994).
[24] P. A. Aitchison, J. N. Chapman, D. B. Jardine, and J. E. Evetts, J. Appl. Phys. **81**, 3775 (1997).
[25] N. Persat, H. A. M. van den Berg, and A. Dinia, J. Magn. Magn. Mater. **165**, 446 (1997).
[26] S. C. Ma, C. K. Lo, Y. D. Yao, D. Y. Chiang, T. F. Ying, and D. R. Huang, J. Magn. Magn. Mater. **209**, 131 (2000).
[27] H. Fujiwara, T. Ishikawa, and W. D. Doyle, J. Appl. Phys. **75**, 6446 (1994).
[28] J. Sasaki and F. Matsubara, J. Appl. Phys. **87**, 3018 (2000).
[29] H. Holloway and D. J. Kubinski, J. Appl. Phys. **83**, 2705 (1998).
[30] C. H. Marrows, R. Loloee, and B. J. Hickey, J. Magn. Magn. Mater. **184**, 137 (1998).
[31] C. H. Marrows and B. J. Hickey, Phys. Rev. B **59**, 463 (1999).
[32] N. Persat and A. Dinia, Phys. Rev. B **56**, 2676 (1997).
[33] B. D. Cullity, *Introduction to Magnetic Materials* (Addison-Wesley, Reading, MA, 1972), pp. 413–418.
[34] M. S. Cohen, in *The Handbook of Thin Film Technology*, edited by L. I. Maissel and R. Glang (McGraw Hill, New York, 1983 Reissue), Chap. 17, pp. 59–69.
[35] K. De'Bell, A. B. MacIsaac, and J. P. Whitehead, Rev. Mod. Phys. **72**, 225 (2000).